Phasing mechanisms between the in-line and cross-flow vortex-induced vibrations of a long tensioned beam in shear flow

Rémi Bourguet [a,*], George Em Karniadakis [b], Michael S. Triantafyllou [c]

[a] Institut de Mécanique des Fluides de Toulouse, Université de Toulouse and CNRS, Toulouse 31400, France
[b] Division of Applied Mathematics, Brown University, Providence, RI 02912, USA
[c] Department of Mechanical Engineering, Massachusetts Institute of Technology, Cambridge, MA 02139, USA

A B S T R A C T

The mechanisms of phasing between the in-line and cross-flow vortex-induced vibrations of a cylindrical tensioned beam in non-uniform flow are studied by direct numerical simulation. Three types of responses are considered, mono-frequency, narrowband, and broadband multi-frequency vibrations; in all cases, in-line and cross-flow vibration components occurring with a frequency ratio of 2 are phase-locked within regions of wake-body synchronization. The in-line/cross-flow phase difference exhibits a persistent spanwise drift when vibration components present significant traveling-wave behavior; this drift depends linearly on the in-line/cross-flow wavenumber difference, controlled by the beam non-linear dispersion relation and also impacted by the effective added mass variability.

Keywords:
Vortex-induced vibrations
Mono- and multi-frequency responses
In-line/cross-flow response phasing
Lock-in in shear flow
Tensioned beam
Direct numerical simulation

1. Introduction

The vortex formation downstream of a long flexible structure with bluff cross-section immersed in a flowing fluid induces unsteady forces on the body which can result in structural vibrations, both in the cross-flow and in-line directions. The increased fatigue damage and mean drag forces caused by the vortex-induced vibrations (VIV) are major issues in civil and offshore engineering, where slender deformable bodies such as cables or risers are exposed to wind and ocean currents; a detailed physical understanding of this fluid–structure interaction phenomenon is necessary for the prediction of the body responses and the development of VIV suppression techniques. This study focuses on the coupling between the in-line and cross-flow vibrations of a long tensioned beam immersed in a current presenting a non-uniform velocity profile, as often observed in the domain of applications.

The investigation of VIV through the simpler problem of a rigid cylinder oscillating in the cross-flow direction within a uniform oncoming flow has highlighted the importance of the synchronization between the vortex shedding and the body displacement for the occurrence of self-excited, self-limited, large-amplitude vibrations [1–4]. This condition of wake-body synchronization is referred to as *lock-in*. When the cylinder is also allowed to oscillate in the in-line direction, vibrations of smaller amplitudes generally occur in this direction with a frequency ratio of 2 compared to the cross-flow response, leading to figure-eight trajectories [5,6]. Previous works have shown that the phase difference between the in-line and cross-flow motions, which determines the shape of the body trajectories, is related to the spectral content of the fluid forces and to the regularity of the resulting orbits [7,8].

The phasing of the in-line and cross-flow responses is also a significant element for the VIV of long flexible cylinders in non-uniform current. In this context, the structural vibrations are excited by the flow in spanwise regions where the lock-in condition is established and damped in zones where the body oscillation and vortex formation frequencies differ [9]. For structural responses dominated by a single vibration frequency in each direction, the lock-in regions are characterized by figure-eight trajectories with a particular orientation [10–12]. Hence the phase difference between the in-line and cross-flow oscillations is closely connected to the energy transfer between the fluid and the structure. Another feature reported in these studies is the occurrence of a spanwise drift of the in-line/cross-flow response phase difference which is associated with a continuous change of the cylinder orbit along its length. This drift may alter the spatial pattern of wake-body synchronization and thus impact the distribution of the regions of structure excitation and damping. Within a sheared current, the possible occurrence of the lock-in condition at different spanwise locations can lead to responses at several frequencies; both

* Corresponding author. Tel.: +33 534322931.
E-mail addresses: bourguet@mit.edu, bourguet@imft.fr (R. Bourguet).

narrowband and broadband multi-frequency vibrations, involving simultaneously high and low structural wavenumbers, may develop depending among others, on the shape of the oncoming flow velocity profile [13–16].

Although previous studies have highlighted typical behaviors in the coupling between the in-line and cross-flow VIV of slender flexible bodies, the underlying mechanisms governing the response phasing remain to be elucidated. In addition, previous works have identified comparable trends in the in-line/cross-flow phasing of the mono-frequency and narrowband multi-frequency responses but further investigation is required to establish whether the same coupling phenomena apply to the different types of responses, including broadband VIV. These aspects are addressed in the present study which aims at analyzing and comparing the mechanisms of synchronization between the in-line and cross-flow responses of a long flexible cylinder subject to mono-frequency as well as narrowband and broadband multi-frequency VIV in sheared current. Direct numerical simulation is employed to predict the flow past a tensioned beam of length to diameter aspect ratio 200, at a Reynolds number equal to 330; different shear profiles and structural properties are considered to promote responses characterized by distinct frequency bandwidths. For each type of structural responses, particular attention is paid to the phasing of the body displacements in the regions of lock-in and to the phenomenon of spanwise drift of the vibration phase difference.

2. Fluid–structure model and numerical method

A tensioned beam of circular cross-section and aspect ratio $L/D = 200$, where L is the beam length and D its diameter, is immersed in a current which is parallel to the global x axis and sheared along the global z axis. A sketch of the physical configuration is presented in Fig. 1(a). The beam is pinned at both ends and free to move in the in-line (x) and cross-flow (y) directions.

The beam mass ratio is defined as $m = \rho_c/\rho_f D^2$, where ρ_c is its mass per unit length and ρ_f the fluid density. In the following, all the physical variables are non-dimensionalized by D and the maximum inflow velocity U. The constant tension, bending stiffness, and damping of the structure are designated by T, EI and K, respectively. The in-line and cross-flow displacements of the body are denoted by ζ_x and ζ_y. The sectional in-line and cross-flow force coefficients are defined as $C_x = 2\ F_x/\rho_f D\ U^2$ and $C_y = 2F_y/\rho_f D\ U^2$, where F_x and F_y are the in-line and cross-flow dimensional sectional fluid forces. The structural dynamics are governed by the following model [17]:

$$\frac{\partial^2 \zeta_{\{x,y\}}}{\partial t^2} - \omega_c^2 \frac{\partial^2 \zeta_{\{x,y\}}}{\partial z^2} + \omega_b^2 \frac{\partial^4 \zeta_{\{x,y\}}}{\partial z^4} + \frac{K}{m}\frac{\partial \zeta_{\{x,y\}}}{\partial t} = \frac{C_{\{x,y\}}}{2m}. \tag{1}$$

t denotes the non-dimensional time variable. ω_c and ω_b denote the cable and beam phase velocities, defined as $\omega_c^2 = T/m$ and $\omega_b^2 = EI/m$, respectively. The structural damping is set equal to zero ($K = 0$) to allow maximum amplitude oscillations. The flow around the tensioned beam is predicted using the direct numerical simulation of the three-dimensional incompressible Navier–Stokes equations.

Two specific sheared inflow velocity profiles are considered: a profile with linearly varying velocity as function of z is employed in reference to previous experimental and numerical studies; an exponentially sheared profile, which represents a more realistic profile in the context of offshore applications, i.e. vertical risers or mooring lines immersed in ocean currents, is also considered. The velocity profiles are plotted in Fig. 1(b). For both profiles, the maximum inflow velocity U occurs at $z = 0$ and the ratio between the maximum and minimum inflow velocities is set to 3.67. The Reynolds number (Re) based on D and U is equal to 330. These inflow velocity profiles associated with different values of the structural properties result in three distinct types of body responses, as described in Section 3.1. The selected parameters reported in Table 1, lead to vibrations involving high structural wavenumbers in all three cases; such vibrations are representative of configurations encountered in the context of ocean engineering [18,19,10]. In the linear inflow velocity case when the mass ratio value changes from 3 to 6, while ω_c and ω_b are kept constant, this induces an alteration of the time-averaged in-line bending of the structure and thus a change in the inflow velocity profile normal to the beam. As reported in a previous work [15], this change results in a transition between mono-frequency and multi-frequency vibrations. The exponential velocity profile is the same as the profile employed in [14], where multi-frequency VIV, characterized by a wider range of excited frequencies than in the linear shear case, have been noted.

The coupled fluid–structure system is solved by the parallelized code *Nektar*, which is based on the spectral/*hp* element method [20]. The version of the code employs a hybrid scheme with Fourier expansion in the spanwise (z) direction and Jacobi-Galerkin formulation in the (x,y) planes. A boundary-fitted coordinate formulation is used to take into account the cylinder deformation. Details concerning time integration schemes and validation of the numerical method have been reported in [21] and [17]. The computational domain (50D downstream and 20D in front, above, and below the cylinder) and discretization (2175 elements with polynomial order 7 in the (x,y) planes and 512 complex Fourier modes in the z direction) are the same as in [9]. A no-slip condition is applied on the cylinder surface. Following a technique validated in the above mentioned reference, a buffer region (not presented in the following) is used to enforce the periodicity of the inflow velocity profile implied by the Fourier expansion used in the z direction. The analysis is based on time series of more than 300 time units, collected after convergence of the time-averaged in-line displacement of the beam, for each simulation.

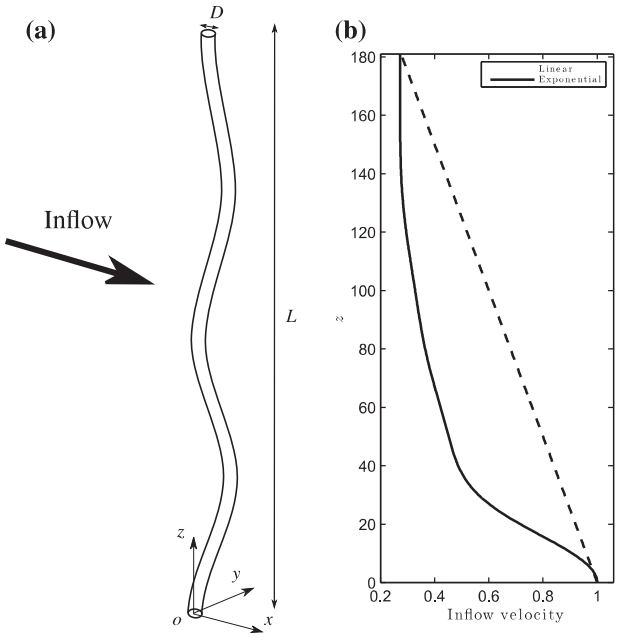

Fig. 1. (a) Sketch of the physical configuration. (b) Linear and exponential inflow velocity profiles.

Table 1
Fluid–structure model parameters and structural response characteristics.

Case	Velocity profile	m	ω_c	ω_b	Cross-flow frequency	Cross-flow wavenumber	In-line wavenumber
Mono-frequency	Linear	3	4.55	9.09	0.154	0.0355	0.06
Narrowband	Linear	6	4.55	9.09	0.149	0.0325	0.0565
					0.162	0.035	0.06
					0.174	0.0375	0.065
Broadband	Exponential	6	5	10	0.048	0.01	0.019
					0.083	0.0175	0.0325
					0.095	0.02	0.0375
					0.162	0.0325	0.056

3. Results and discussion

The body responses are described in Section 3.1. The link between the occurrence of the wake-body synchronization condition and the phasing of the in-line and cross-flow vibrations is examined in Section 3.2. The drift of the in-line/cross-flow response phase difference is analyzed in Section 3.3.

3.1. Three types of structural responses in shear flow

Three distinct types of vortex-induced responses of the tensioned beam are identified and analyzed in this section. The typical vibrational responses of the beam are illustrated in Fig. 2 through selected time series of the cross-flow displacement along the span. In all three cases the vibrations present mixed standing-traveling wave patterns. The change in the nature of the response among the three cases, which can be observed qualitatively in Fig. 2, is quantified by means of spatio-temporal spectral analysis. The power spectral density (PSD) of the body displacement is plotted as a function of the temporal frequency and spatial wavenumber in Fig. 3, separately for each case. Positive frequencies are considered in these plots, negative spatial wavenumbers are thus associated with structural waves traveling in the direction of increasing z, from the high to the low-inflow velocity regions; positive wavenumbers correspond to waves traveling in the other direction.

In linear shear flow (Fig. 3(a) and (b)), as previously mentioned, the modification of the mean curvature of the structure, as m is changed from 3 to 6, induces a switch from a vibration at a single frequency along the span to a response involving several frequencies [15]. The three frequencies excited for $m = 6$ are contained within a narrow band and the corresponding spatial wavenumbers can be associated with three adjacent sine Fourier modes, $n \in \{13, 14, 15\}$ with the nth mode defined as $\sin(\pi n\, z\, D/L)$. Within exponential shear flow, the beam exhibits a vibrational response involving a broad range of frequencies, associated with both low and high structural wavenumbers (Fig. 3(c)); the excited wavenumbers can be related to sine Fourier modes in the range $n \in \{4, 7, 8, 13\}$. As generally observed in this context, each component of the response in the cross-flow direction is accompanied by a component occurring with a frequency ratio of 2 in the in-line direction. The change in the spectral content of the cross-flow response, identified among the three cases, is also noted in the in-line direction. In the following, these three types of responses are referred to as *mono-frequency*, *narrowband*, and *broadband*, as also shown in Table 1.

Each excited frequency is principally associated with a single spatial wavelength, which is generally the same in the negative and positive-wavenumber spectra. The relative weights of the positive and negative-wavenumber PSD peaks characterize the standing or traveling nature of the corresponding wave. The high-wavenumber vibration components exhibit a pronounced traveling-wave behavior oriented towards the low-velocity region, as indicated by the larger magnitudes of the PSD peaks located on the negative-wavenumber side of the spectra. A similar behavior

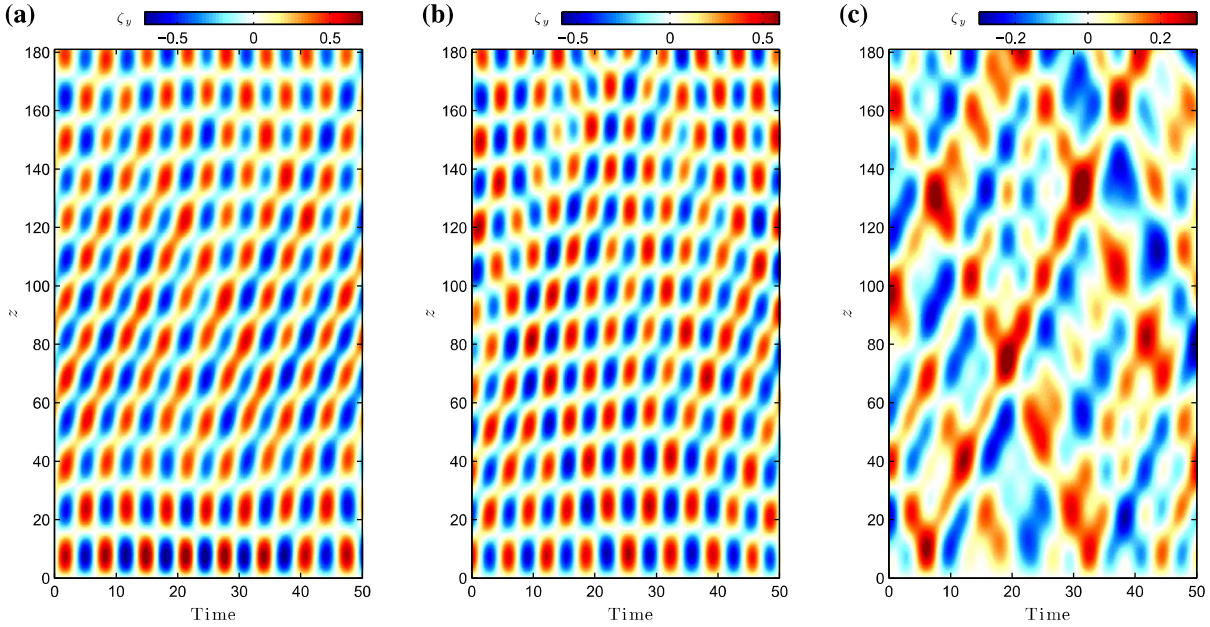

Fig. 2. Selected time series of the cross-flow displacement along the span, (a,b) in the linear shear case for (a) $m = 3$ (mono-frequency response) and (b) $m = 6$ (narrowband response), and (c) in the exponential shear case ($m = 6$, broadband response).

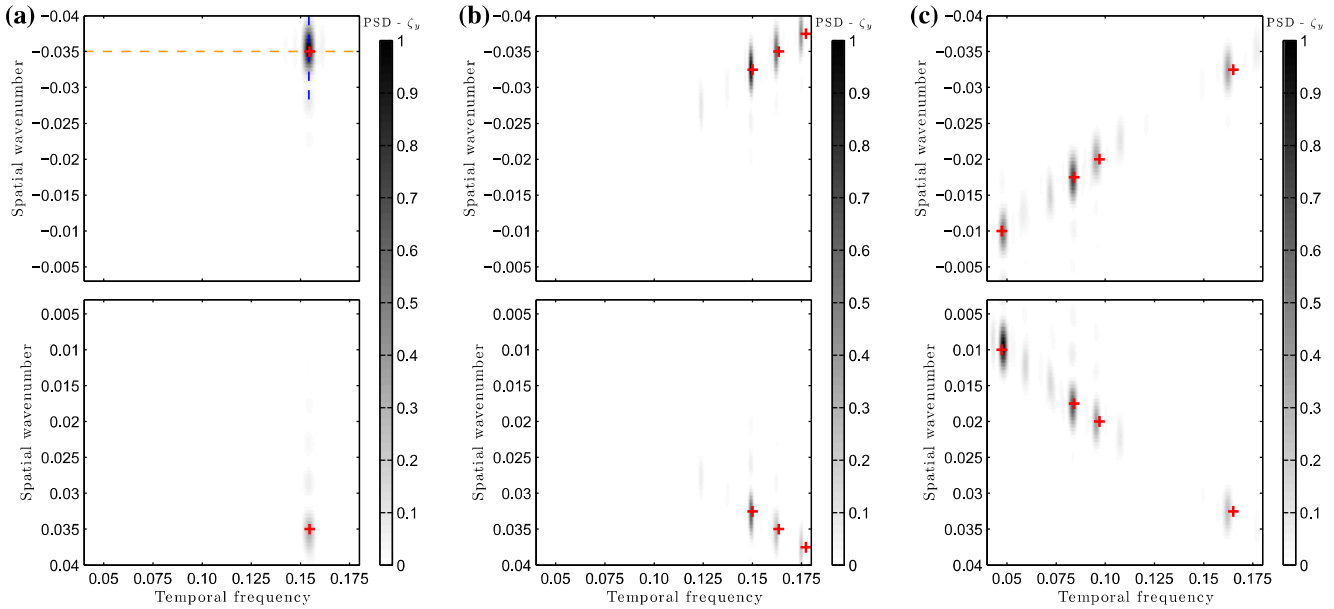

Fig. 3. Spatio-temporal spectral analysis of the cross-flow displacement, (a, b) in the linear shear case for (a) $m = 3$ (mono-frequency response) and (b) $m = 6$ (narrowband response), and (c) in the exponential shear case ($m = 6$, broadband response). The predominant vibration frequencies are identified by blue vertical dashed lines. Structural wavenumbers associated with selected sine Fourier modes are indicated by orange horizontal dashed lines; (a) $n = 14$, (b) $n \in \{13,14,15\}$, (c) $n \in \{4,7,8,13\}$. Red crosses denote the natural frequencies associated with these wavenumbers. (For interpretation of the references to colour in this figure legend, the reader is referred to the web version of this article.)

is observed in the in-line direction. This trend can be linked to the spanwise distribution of the excitation and damping regions of the beam by the flow, as discussed in Section 3.2. The predominant cross-flow vibration frequencies and corresponding excited wavenumbers are indicated in Table 1, as well as the wavenumbers excited in the in-line direction with a frequency ratio of 2; the absolute values of the wavenumbers are reported in this table. As previously noted [9], the actual response peaks may present significant departures from the natural frequencies issued from the tensioned beam dispersion relation modified by considering an added mass coefficient equal to 1 (red crosses in Fig. 3). This phenomenon can be related to the variability of the effective added mass that modulates the relation between excited frequencies and wavenumbers [16].

The root mean square (RMS) values of the structural response amplitudes along the beam span are plotted in Fig. 4. In these plots and in the following the deviation of the in-line response from its time-averaged value $\tilde{\zeta}_x$ is considered. As reported in previous studies involving flexible cylinders (e.g. [22,19]), the amplitudes of vibration are smaller in the in-line direction, as also observed for elastically-mounted rigid cylinders. The reduction of the cross-flow response amplitude in the case of broadband vibrations (exponential inflow profile) is in agreement with the observations of [14] concerning a flexible cylinder constrained to oscillate in the cross-flow direction within similar currents; the cross-flow response amplitudes are comparable to those reported in this previous study.

The synchronization between the in-line and cross-flow responses of the beam is analyzed in the next section, in relation with the occurrence of the wake-body synchronization condition along the span.

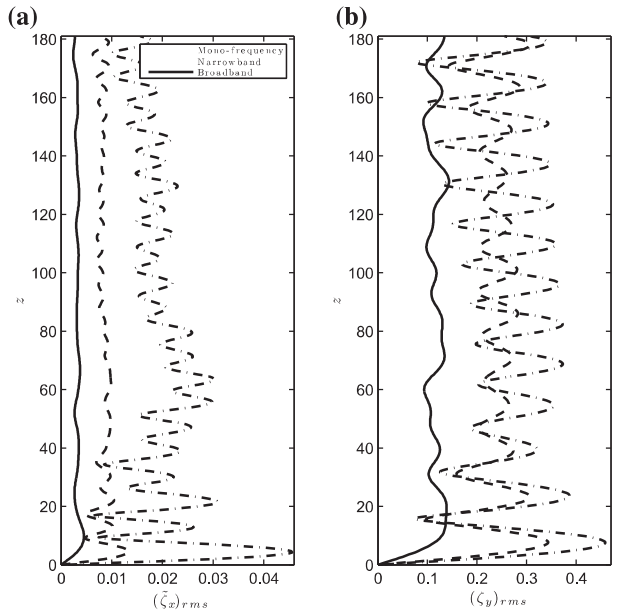

Fig. 4. RMS values of the (a) in-line displacement fluctuation and (b) cross-flow displacement, along the span.

3.2. Phase-locking of the in-line and cross-flow responses under wake-body synchronization

For an elastically-mounted rigid cylinder placed in uniform current, a clear link has been identified between the occurrence of large-amplitude repeatable vibrations and the orientation of the figure-eight trajectories of the body: counter-clockwise orbits, in which the cylinder moves upstream at the extrema of its cross-flow oscillation, induce larger vorticity generation and lead to a particular phasing between the body motion and the vortex suction forces, resulting in stable vibrations [7,8]. For a long flexible cylinder immersed in sheared current and presenting a single vibration frequency in each direction, the condition of wake-body synchronization is generally connected with this particular type of trajectories [10–12]. The synchronization of the in-line and cross-flow vibrations in the regions of lock-in is examined in this section for the mono-frequency, narrowband and broadband response cases identified in Section 3.1.

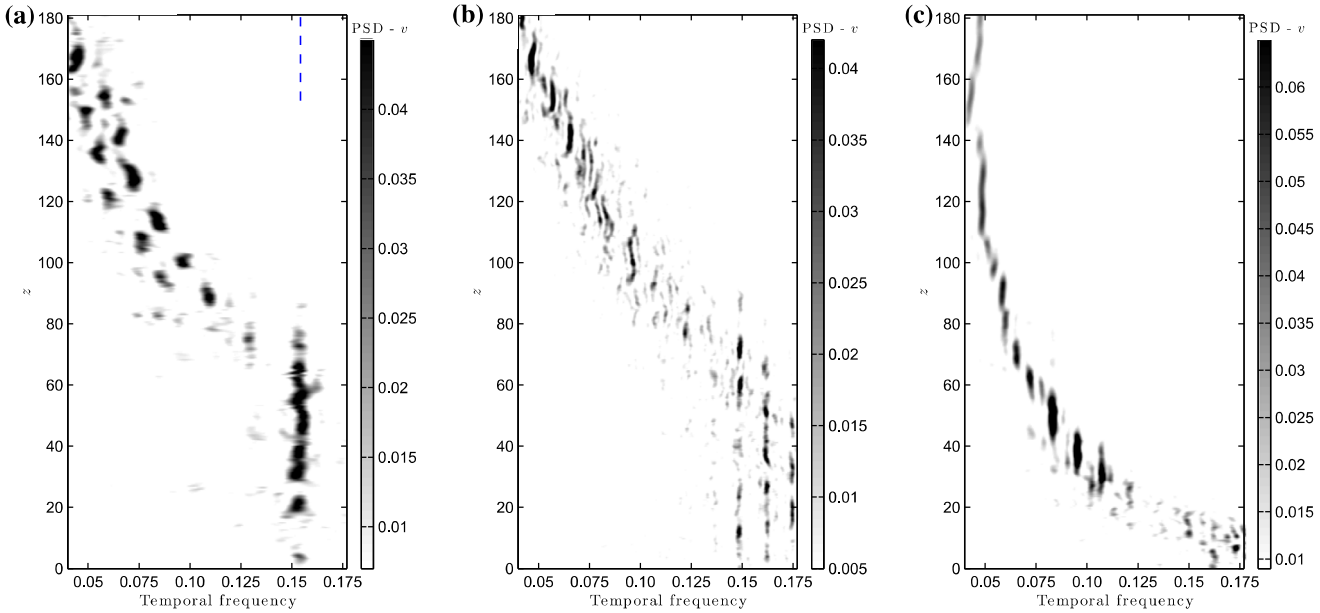

Fig. 5. PSD of the cross-flow component of flow velocity along a spanwise line in the wake, in the (a) mono-frequency, (b) narrowband, and (c) broadband response cases. Blue dashed lines indicate the predominant frequencies of the cross-flow vibrations identified in Fig. 3. (For interpretation of the references to colour in this figure legend, the reader is referred to the web version of this article.)

For a slender deformable body, the lock-in condition is defined at each spanwise location by the synchronization between the local frequency of the vortex formation and the local frequency of the cross-flow structural vibration; the absence of wake-body synchronization is referred to as the non-lock-in condition. The occurrence of the lock-in condition along the beam length is monitored by comparing the PSD of the cross-flow component of the flow velocity in the wake to the predominant vibration frequencies previously identified, as shown in Fig. 5. In the three cases, the wake exhibits a discontinuous pattern composed of cells of constant vortex shedding frequency, as also noted for stationary cylinders with varying spanwise conditions (e.g. [23–25]). In the mono-frequency and narrowband multi-frequency response cases (Fig. 5(a) and (b)), the lock-in condition occurs on the high-inflow velocity side, over similar spanwise extents, while vortex shedding and body oscillation are not synchronized on the rest of the span. In contrast, the broadband vibration case (Fig. 5(c)) is characterized by a distribution of the lock-in condition which occurs both in the high and low-velocity regions.

The high-wavenumber vibration components are excited by the flow under the lock-in condition in the high-velocity region and are damped in the low-velocity zone; this explains the preferential orientation of the corresponding structural waves which are moving in the direction of increasing z, as noted in Section 3.1.

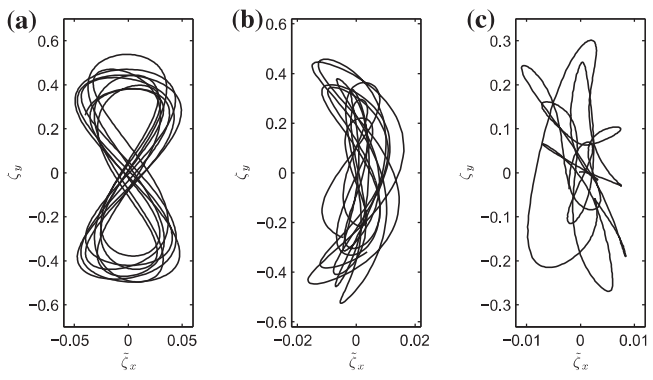

Fig. 6. Selected trajectories of the beam over 50 time units, in the (a) mono-frequency ($z = 38$), (b) narrowband ($z = 50$) and (c) broadband ($z = 71$) response cases.

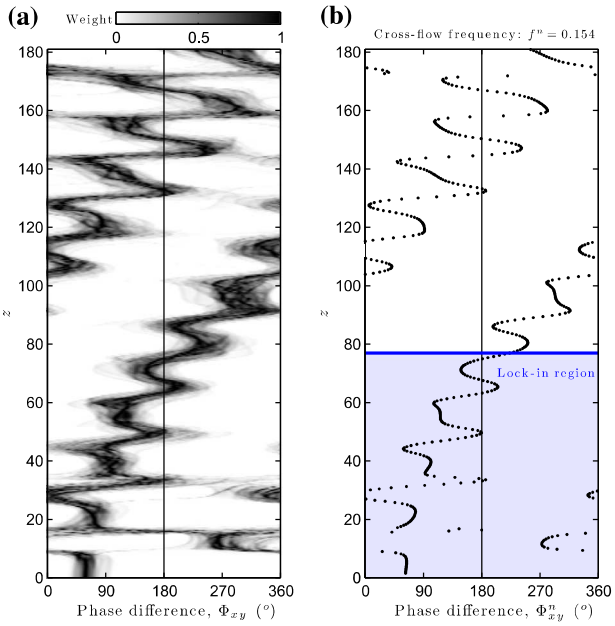

Fig. 7. Phase difference between the in-line and cross-flow displacements along the span, in the case of mono-frequency responses: (a) histogram issued from the total displacement signals (Φ_{xy} defined in (2)) and (b) difference between the spatial phases of the principal components of the displacements presenting a frequency ratio of 2 (Φ^n_{xy} defined in (4)); predominant cross-flow vibration frequency identified in Fig. 3(a), $f^n = 0.154$. The limit between counter-clockwise and clockwise orbits (180°) is indicated by a black vertical line. In (b), the lock-in region is colored in blue; the phase difference in the case of pure traveling waves, based on the effective excited wavenumbers, is indicated by a red dashed line. (For interpretation of the references to colour in this figure legend, the reader is referred to the web version of this article.)

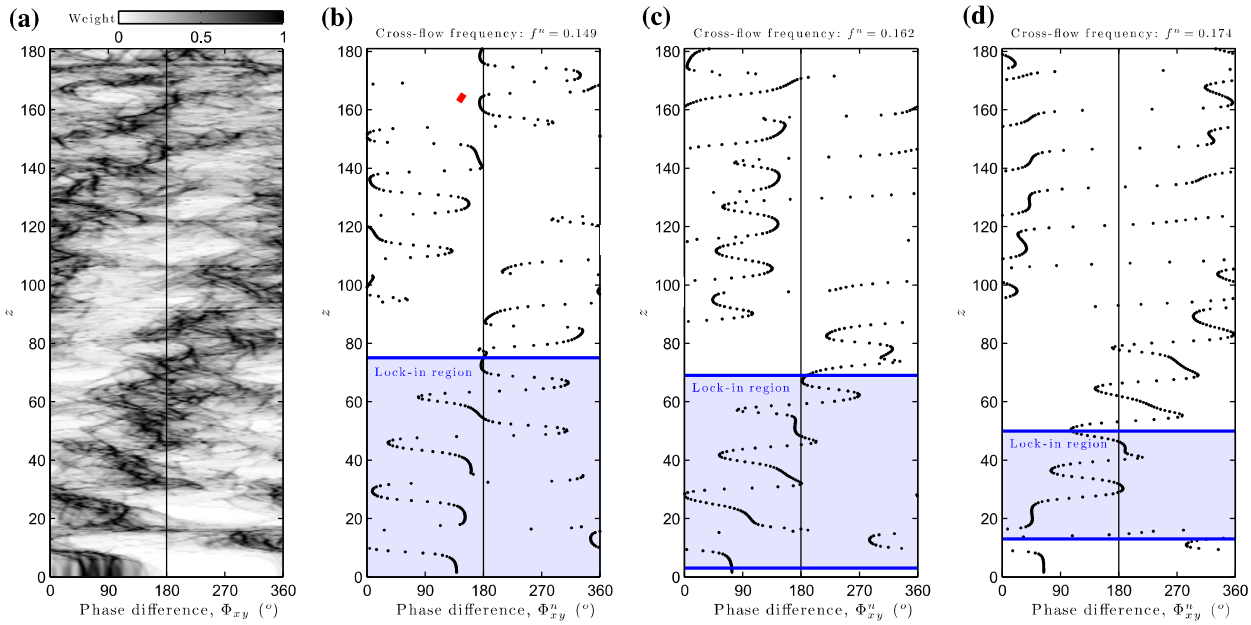

Fig. 8. Phase difference between the in-line and cross-flow displacements along the span, in the case of narrowband responses: (a) histogram issued from the total displacement signals (Φ_{xy} defined in (2)) and (b–d) difference between the spatial phases of the principal components of the displacements presenting a frequency ratio of 2 (Φ^n_{xy} defined in (4)); predominant cross-flow vibration frequencies identified in Fig. 3(b), (b) $f^n = 0.149$, (c) $f^n = 0.162$, (d) $f^n = 0.174$. The limit between counter-clockwise and clockwise orbits in the case of mono-frequency responses (180°) is indicated by a black vertical line. In (b–d), the lock-in region associated with each vibration frequency is colored in blue; the phase difference in the case of pure traveling waves, based on the effective excited wavenumbers, is indicated by a red dashed line. (For interpretation of the references to colour in this figure legend, the reader is referred to the web version of this article.)

Selected trajectories of the beam in the three cases under study are presented in Fig. 6. The phase difference between the in-line and cross-flow displacements can be defined by:

$$\Phi_{xy} = p\phi_x - q\phi_y, \tag{2}$$

where ϕ_x and ϕ_y are the instantaneous phases of the in-line and cross-flow responses; p and q are two integer numbers defining the level of synchronization. The couple $(p,q) = (1,2)$ is chosen here since the synchronization is investigated for a frequency ratio of 2 between the responses in each direction. For mono-frequency vibrations, $\Phi_{xy} \in [0°, 180°]$ corresponds to counter-clockwise orbits, in contrast to the trajectories in the opposite direction, where the body moves downstream at the extrema of its cross-flow displacement, referred to as clockwise ($\Phi_{xy} \in [180°, 360°]$) [7]. The histogram of Φ_{xy} based on the instantaneous phases determined by the Hilbert transform of the displacement signals are plotted along the span in the mono-frequency and narrowband response cases in Figs. 7(a) and 8(a), respectively. In spite of the change in the nature of the structural response, both cases exhibit very similar trends, with a phase difference generally lower than 180° in the high-velocity region and a clear spanwise drift towards higher angles as z increases. These two aspects are analyzed in the following.

For a better identification of the synchronization patterns of the in-line and cross-flow vibrations, especially in the cases where several frequencies are involved in the structural responses in each direction, the displacements can be approximated as follows, using $N+1$ temporal Fourier modes:

$$\begin{aligned}\zeta_{\{x,y\}}(z,t) &\approx \sum_{n=-N/2}^{N/2} a^n_{\{x,y\}}(z)\exp(2\pi i f^n t) \\ &= \sum_{n=-N/2}^{N/2} \left|a^n_{\{x,y\}}\right|(z)\exp\left(i\left(2\pi f^n t + \psi^n_{\{x,y\}}(z)\right)\right),\end{aligned} \tag{3}$$

where $f^n = n/T_s$ and T_s is the sampling period. The complex modal coefficients a^n_x and a^n_y are written in terms of their moduli and their spatial phases ψ^n_x and ψ^n_y. The phase difference between the in-line and cross-flow responses occurring at frequencies $2f^n$ and f^n respectively, is evaluated as follows:

$$\Phi^n_{xy} = \psi^{2n}_x - 2\psi^n_y. \tag{4}$$

The spanwise evolutions of the phase differences associated with the predominant cross-flow vibration frequencies for the mono-frequency, narrowband and broadband response cases are plotted in Figs. 7(b), 8(b–d) and 9, respectively. In these figures, the lock-in regions including all the locations locally locked-in at the studied frequency are indicated in blue.[1] In all cases and for each excited frequency, it can be noted that the phase difference remains principally lower than 180° within the lock-in region. As a consequence, the in-line and cross-flow vibration components locally involved in the wake-body synchronization condition, are locked within a specific range of phase difference angles, even if the beam trajectories substantially differ from figure-eight orbits, as illustrated in Fig. 6. This phase-locking mechanism, previously associated with observations of a particular trajectory orientation within the lock-in region in the mono-frequency case, thus extends to the multi-frequency vibrations, including the case of broadband responses.

A spanwise drift of the phase difference between the high-wavenumber components of the in-line and cross-flow vibrations can be noted in all studied cases, both within and outside the lock-in regions and regardless of the spectral content of the responses; this drift is investigated in the next section.

3.3. Spanwise drift of the phase difference between the in-line and cross-flow responses

The drift of the in-line/cross-flow response phase difference identified in the previous section has also been observed in field

[1] For interpretation of color in Figs. 9 and 10, the reader is referred to the web version of this article.

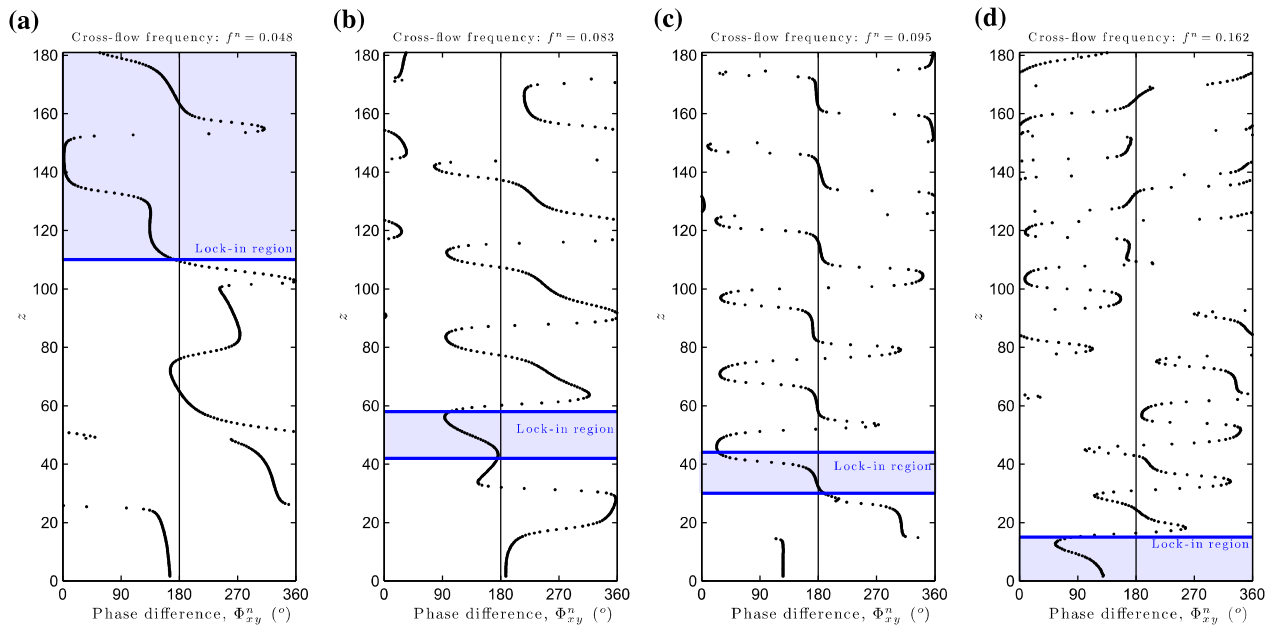

Fig. 9. Phase difference between the in-line and cross-flow displacements along the span, in the case of broadband responses: difference between the spatial phases of the principal components of the displacements presenting a frequency ratio of 2 (Φ^n_{xy} defined in (4)); predominant cross-flow vibration frequencies identified in Fig. 3(c), (a) $f^n = 0.048$, (b) $f^n = 0.083$, (c) $f^n = 0.095$, (d) $f^n = 0.162$. The limit between counter-clockwise and clockwise orbits in the case of mono-frequency responses (180°) is indicated by a black vertical line. The lock-in region associated with each vibration frequency is colored in blue. In (d), the phase difference in the case of pure traveling waves, based on the effective excited wavenumbers, is indicated by a red dashed line. (For interpretation of the references to colour in this figure legend, the reader is referred to the web version of this article.)

experiments where a continuous alteration of the body trajectory shape along its length has been reported [10].

To clarify the mechanisms driving the phase difference drift, a model composed of a mixed standing-traveling wave in each direction is defined as follows:

$$\zeta_{\{x,y\}}(z,t) = a^+_{\{x,y\}} \cos\left(2\pi f_{\{x,y\}} t + 2\pi k^+_{\{x,y\}} z + \eta^+_{\{x,y\}}\right) + a^-_{\{x,y\}} \cos\left(2\pi f_{\{x,y\}} t + 2\pi k^-_{\{x,y\}} z + \eta^-_{\{x,y\}}\right). \quad (5)$$

f_x and f_y are the in-line and cross-flow vibration frequencies, with $f_x = 2f_y > 0$. k^+_x and k^+_y denote the in-line and cross-flow excited wavenumbers associated with waves traveling in the direction of decreasing $z\left(k^+_{\{x,y\}} > 0\right)$; k^-_x and k^-_y are associated with waves traveling in the other direction $\left(k^-_{\{x,y\}} < 0\right)$. $\eta^+_{\{x,y\}}$ and $\eta^-_{\{x,y\}}$ denote phase lags. $a^+_{\{x,y\}} \geqslant 0$ and $a^-_{\{x,y\}} \geqslant 0$ are the wave amplitudes. The displacements (5) can also be expressed as follows:

$$\zeta_{\{x,y\}}(z,t) = r_{\{x,y\}}(z)\cos(2\pi f_{\{x,y\}} t + \psi_{\{x,y\}}(z)), \quad (6)$$

where

$$r_{\{x,y\}}(z) = \left[2a^+_{\{x,y\}} a^-_{\{x,y\}} \cos\left(2\pi\left(k^+_{\{x,y\}} - k^-_{\{x,y\}}\right)z + \eta^+_{\{x,y\}} - \eta^-_{\{x,y\}}\right) + \left(a^+_{\{x,y\}}\right)^2 + \left(a^-_{\{x,y\}}\right)^2\right]^{1/2} \quad (7)$$

and

$$\psi_{\{x,y\}}(z) = \mathrm{atan2}\left[a^+_{\{x,y\}} \sin\left(2\pi k^+_{\{x,y\}} z + \eta^+_{\{x,y\}}\right) + a^-_{\{x,y\}} \sin\left(2\pi k^-_{\{x,y\}} z + \eta^-_{\{x,y\}}\right), a^+_{\{x,y\}} \cos\left(2\pi k^+_{\{x,y\}} z + \eta^+_{\{x,y\}}\right) + a^-_{\{x,y\}} \cos\left(2\pi k^-_{\{x,y\}} z + \eta^-_{\{x,y\}}\right)\right]. \quad (8)$$

The phase difference between the in-line and cross-flow displacements (5) is thus independent of time:

$$\Phi_{xy} = \psi_x - 2\psi_y. \quad (9)$$

In the case of pure traveling waves oriented in the direction of increasing z ($a^+_{\{x,y\}} = 0$ and $a^-_{\{x,y\}} > 0$), the phase difference becomes:

$$\Phi_{xy}(z,t) = 2\pi\left(k^-_x - 2k^-_y\right)z + \eta^-_x - 2\eta^-_y. \quad (10)$$

As a consequence, for pure traveling waves, the spanwise drift of the phase difference depends linearly on the difference between the in-line wavenumber and a value equal to twice the cross-flow wavenumber.

In the case of pure standing waves ($a^+_{\{x,y\}} = a^-_{\{x,y\}}$ and $k^+_{\{x,y\}} = -k^-_{\{x,y\}}$) the displacements (5) can be expressed as:

$$\zeta_{\{x,y\}}(z,t) = 2a^+_{\{x,y\}} \cos\left(2\pi f_{\{x,y\}} t + \frac{\eta^+_{\{x,y\}} + \eta^-_{\{x,y\}}}{2}\right) \times \cos\left(2\pi k^+_{\{x,y\}} z + \frac{\eta^+_{\{x,y\}} - \eta^-_{\{x,y\}}}{2}\right). \quad (11)$$

The nodes of the in-line and cross-flow standing-wave responses (11) are located at:

$$z \in N_{\{x,y\}} = \left\{\frac{1}{4k^+_{\{x,y\}}}\left(1 + 2n - \frac{\eta^+_{\{x,y\}} - \eta^-_{\{x,y\}}}{\pi}\right), n \in \mathbb{Z}\right\}. \quad (12)$$

For pure standing waves, the spatial phases can be expressed as:

$$\psi_{\{x,y\}}(z) = \mathrm{atan2}\left[\sin\left(\frac{\eta^+_{\{x,y\}} + \eta^-_{\{x,y\}}}{2}\right)\cos\left(2\pi k^+_{\{x,y\}} z + \frac{\eta^+_{\{x,y\}} - \eta^-_{\{x,y\}}}{2}\right), \cos\left(\frac{\eta^+_{\{x,y\}} + \eta^-_{\{x,y\}}}{2}\right)\cos\left(2\pi k^+_{\{x,y\}} z + \frac{\eta^+_{\{x,y\}} - \eta^-_{\{x,y\}}}{2}\right)\right] \quad (13)$$

and the phase difference becomes, for $z \notin N_{\{x,y\}}$:

$$\Phi_{xy}(z,t) = \frac{\eta^+_x + \eta^-_x}{2} - \eta^+_y - \eta^-_y + \Pi(z), \quad (14)$$

where

$$\Pi(z) = \begin{cases} \pi \text{ for } z \in \bigcup\limits_{n\in\mathbb{Z}} \left]\frac{1}{4k_x^+}\left(1+4n-\frac{\eta_x^+-\eta_x^-}{\pi}\right), \frac{1}{4k_x^+}\left(3+4n-\frac{\eta_x^+-\eta_x^-}{\pi}\right)\right[, \\ 0 \text{ for } z \in \bigcup\limits_{n\in\mathbb{Z}} \left]\frac{1}{4k_x^+}\left(3+4n-\frac{\eta_x^+-\eta_x^-}{\pi}\right), \frac{1}{4k_x^+}\left(5+4n-\frac{\eta_x^+-\eta_x^-}{\pi}\right)\right[. \end{cases} \quad (15)$$

As a result, the phase difference exhibits a discontinuous evolution corresponding to an alternating clockwise/counter-clockwise spanwise pattern; the transitions between the two types of orbits occur at the nodes of the in-line response.

In order to illustrate the typical behaviors of the phase difference, the spanwise evolutions of Φ_{xy} determined through (9) in the cases of pure standing waves, pure traveling waves (oriented in the direction of increasing z) and mixed responses are plotted in Fig. 10. In Fig. 10(a), the cross-flow response wavenumber is that identified in the mono-frequency response case (Table 1) and a ratio of 2 is selected between the in-line and cross-flow wavenumbers, $k_x^+ = 2k_y^+$ and $k_x^- = 2k_y^-$; the phase lags are chosen arbitrarily.

For pure standing waves in each direction, the phase difference is characterized by a discontinuous spanwise pattern (blue triangles), as shown in the above analysis. In the case of pure traveling waves, due to the ratio of 2 between the in-line and cross-flow excited wavenumbers, Φ_{xy} is constant along the beam length (red dashed line), as expected from (10). In the mixed response case where the relative magnitudes of the positive and negative-wavenumber domain contributions match the values of the mono-frequency response case (Fig. 3(a)), the phase difference presents a zig-zagging behavior centered about the pure traveling wave evolution (black dots).

If the in-line and cross-flow vibration wavenumbers identified by spectral analysis in the mono-frequency response case are considered (Table 1), the phase difference exhibits the evolutions presented in Fig. 10(b). The spanwise drift of Φ_{xy} observed in the case of mixed standing-traveling waves (black dots) follows rigorously the trend of pure traveling wave responses (red dashed line), the sawtooth behavior being induced by the underlying standing wave patterns.

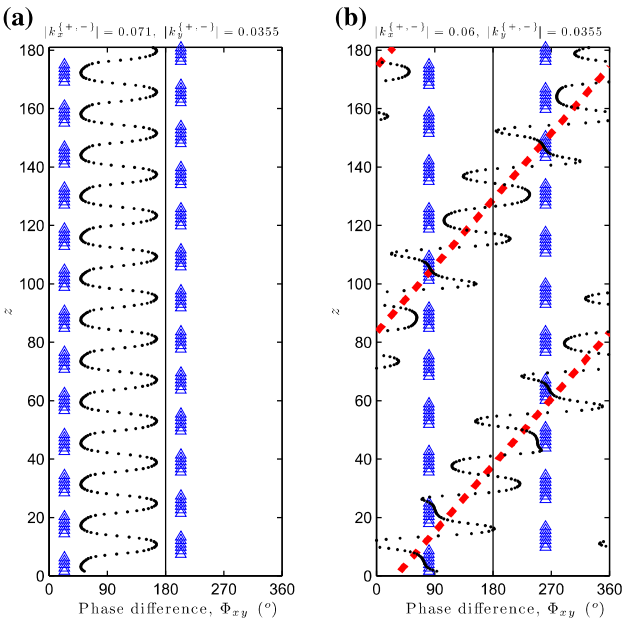

Fig. 10. Phase difference between the in-line and cross-flow displacements along the span, for the model (5), with an in-line to cross-flow wavenumber ratio (a) equal to 2 and (b) different from 2. The phase differences in the cases of pure standing waves, pure traveling waves and mixed responses are denoted by blue triangles, red dashed lines and black dots, respectively. The limit between counter-clockwise and clockwise orbits (180°) is indicated by a black vertical line. (For interpretation of the references to colour in this figure legend, the reader is referred to the web version of this article.)

The spanwise evolutions of the phase differences for pure traveling waves, based on the predominant excited wavenumbers in the three cases under study, are indicated by red dashed lines for each pair of in-line/cross-flow responses involving high structural wavenumbers in Figs. 7(b), 8(b–d) and 9(d). As also noted with the model (5), the actual phase differences follow the pure traveling wave behaviors, except in zones dominated by standing waves (for example near $z = 0$ in Fig. 7(b)), where the previously described discontinuous pattern is observed. No phase difference drift is observed for the vibration components involving lower spatial wavenumbers which present a strong standing wave nature.

The drift of the phase difference between the in-line and cross-flow vibration components presenting a frequency ratio of 2, occurs in regions of traveling waves where the ratio of in-line to cross-flow excited wavenumbers differs from 2. The high-wavenumber structural responses exhibit a well-defined traveling-wave behavior as noted in Section 3.1. In addition, for a tensioned beam, a ratio different from 2 between the in-line and cross-flow excited wavenumbers is expected, due to the non-linear dispersion relation that links excited frequencies and wavenumbers in vacuum [9]. When such body vibrates within a current, the variability of the effective added mass may modify the frequency/wavenumber relation [16] and thus alter the phase difference drift. It should be mentioned that even for a body characterized by a linear dispersion relation in vacuum, such as a tension-dominated structure, the possible differences of effective added mass in the in-line and cross-flow directions may induce a deviation from the wavenumber ratio of 2 and thus result in a spanwise drift of the phase difference.

4. Conclusions

The synchronization between the in-line and cross-flow vortex-induced vibrations of a long tensioned beam placed in sheared current has been studied by means of direct numerical simulation. Two inflow velocity profiles and different body properties have been employed to trigger three distinct types of structural responses: *mono-frequency* vibrations characterized by a single frequency excited in each direction, and multi-frequency vibrations, involving either a *narrowband*, or a *broadband* set of oscillation frequencies. The change in the response spectral content is accompanied by a modification of the spanwise pattern of wake-body synchronization. The lock-in condition appears on the high-inflow velocity side in the cases of mono-frequency and narrowband responses, resulting in high-wavenumber vibrations. In contrast, in the broadband case, responses that include a wide range of spatial wavenumbers are excited through a distributed occurrence of the lock-in condition along the beam span. In all cases, the body exhibits mixed standing-traveling wave responses, while a frequency ratio of 2 can be established between corresponding in-line and cross-flow vibration components.

Two salient features of the in-line/cross-flow response synchronization have been analyzed.

Within a lock-in region, corresponding in-line and cross-flow vibration components have a phase difference angle that remains in a well-defined range. For mono-frequency responses, this range corresponds to counter-clockwise figure-eight orbits where the structure moves upstream at the extrema of its cross-flow displacement. The mechanism of phase-locking of the vibration components under wake-body synchronization is found to extend to the case of multi-frequency vortex-induced vibrations, including the case of broadband responses, where both high and low wavenumbers are excited: a Fourier expansion of the in-line and

cross-flow responses and the association of in-line to cross-flow components with frequencies in the ratio of 2 to 1, allows the identification of a relative phase difference for each such pair; the phase difference angle is contained within the same range as for mono-frequency responses.

Along the beam span, a persistent drift is noted in the phase difference between corresponding in-line and cross-flow vibration components, which present a frequency ratio of 2 and contain a strong traveling-wave chararacter, i.e. the high-frequency and wavenumber responses. The spanwise evolution of the drifting phase difference is linearly determined by the difference between the in-line excited wavenumber and a value equal to twice the cross-flow excited wavenumber; no drift would be observed if the in-line to cross-flow wavenumber ratio were exactly equal to 2. The departure from a wavenumber ratio of 2 can be attributed to the non-linear dispersion relation of the tensioned beam; the relation between excited frequencies and wavenumbers can be also modulated by the variability of the effective added mass, which may thus impact the spanwise drift.

The present results may have significant implications in the domain of applications, especially for the design of long flexible marine structures exposed to ocean currents. The phase-locking mechanism of the in-line and cross-flow responses in the regions of flow-induced excitation and the connection between the spanwise drift of the phase difference, the occurrence of traveling-wave vibrations and the response frequency/wavenumber relation may be useful insights for the elaboration of VIV reduction strategies, based on flow manipulation but also on optimized structural properties. In addition, the applicability of the same coupling mechanisms, independently of the spectral content of the structural responses, is an important finding for the development of semi-empirical modeling approaches based on short-span rigid cylinder hydrodynamic results and dedicated to VIV prediction and quantification of the associated fatigue damage.

Acknowledgments

The authors wish to acknowledge support from the BP-MIT Major Projects Programme, monitored by M. Tognarelli and P. Beynet; and the Office of Naval Research under Grants N00014-07-1-0135 and N00014-07-1-0446, monitored by T. Swean, Jr.

References

[1] Bearman PW. Vortex shedding from oscillating bluff bodies. Annu Rev Fluid Mech 1984;16:195–222.
[2] Sarpkaya T. A critical review of the intrinsic nature of vortex-induced vibrations. J Fluids Struct 2004;19:389–447.
[3] Williamson CHK, Govardhan R. Vortex-induced vibrations. Annu Rev Fluid Mech 2004;36:413–55.
[4] Leontini JS, Stewart BE, Thompson MC, Hourigan K. Wake state and energy transitions of an oscillating cylinder at low reynolds number. Phys Fluids 2006;18:067101.
[5] Jauvtis N, Williamson CHK. The effect of two degrees of freedom on vortex-induced vibration at low mass and damping. J Fluid Mech 2004;509:23–62.
[6] Singh SP, Mittal S. Vortex-induced oscillations at low reynolds numbers: hysteresis and vortex-shedding modes. J Fluids Struct 2005;20:1085–104.
[7] Dahl JM, Hover FS, Triantafyllou MS, Dong S, Karniadakis GE. Resonant vibrations of bluff bodies cause multivortex shedding and high frequency forces. Phys Rev Lett 2007;99:144503.
[8] Dahl JM, Hover FS, Triantafyllou MS, Oakley OH. Dual resonance in vortex-induced vibrations at subcritical and supercritical Reynolds numbers. J Fluid Mech 2010;643:395–424.
[9] Bourguet R, Karniadakis GE, Triantafyllou MS. Vortex-induced vibrations of a long flexible cylinder in shear flow. J Fluid Mech 2011;677:342–82.
[10] Vandiver JK, Jaiswal V, Jhingran V. Insights on vortex-induced, traveling waves on long risers. J Fluids Struct 2009;25:641–53.
[11] Modarres-Sadeghi Y, Mukundan H, Dahl JM, Hover FS, Triantafyllou MS. The effect of higher harmonic forces on fatigue life of marine risers. J Sound Vibr 2010;329:43–55.
[12] Bourguet R, Modarres-Sadeghi Y, Karniadakis GE, Triantafyllou MS. Wake-body resonance of long flexible structures is dominated by counter-clockwise orbits. Phys Rev Lett 2011;107:134502.
[13] Vandiver JK, Allen D, Li L. The occurrence of lock-in under highly sheared conditions. J Fluids Struct 1996;10:555–61.
[14] Lucor D, Mukundan H, Triantafyllou MS. Riser modal identification in CFD and full-scale experiments. J Fluids Struct 2006;22:905–17.
[15] Bourguet R, Lucor D, Triantafyllou MS. Mono- and multi-frequency vortex-induced vibrations of a long tensioned beam in shear flow. J Fluids Struct 2012;32:52–64.
[16] Bourguet R, Karniadakis GE, Triantafyllou MS. Multi-frequency vortex-induced vibrations of a long tensioned beam in linear and exponential shear flows. J Fluids Struct; in press. http://dx.doi.org/10.1016/j.jfluidstructs.2012.07.007.
[17] Evangelinos C, Karniadakis GE. Dynamics and flow structures in the turbulent wake of rigid and flexible cylinders subject to vortex-induced vibrations. J Fluid Mech 1999;400:91–124.
[18] Trim AD, Braaten H, Lie H, Tognarelli MA. Experimental investigation of vortex-induced vibration of long marine risers. J Fluids Struct 2005;21:335–61.
[19] Lie H, Kaasen KE. Modal analysis of measurements from a large-scale VIV model test of a riser in linearly sheared flow. J Fluids Struct 2006;22:557–75.
[20] Karniadakis GE, Sherwin S. Spectral/hp element methods for CFD. first ed. Oxford: Oxford University Press; 1999.
[21] Newman DJ, Karniadakis GE. A direct numerical simulation study of flow past a freely vibrating cable. J Fluid Mech 1997;344:95–136.
[22] Chaplin JR, Bearman PW, Huera-Huarte FJ, Pattenden RJ. Laboratory measurements of vortex-induced vibrations of a vertical tension riser in a stepped current. J Fluids Struct 2005;21:3–24.
[23] Gaster M. Vortex shedding from circular cylinders at low Reynolds numbers. J Fluid Mech 1971;46:749–56.
[24] Piccirillo PS, Van Atta CW. An experimental study of vortex shedding behind linearly tapered cylinders at low Reynolds number. J Fluid Mech 1993;246:163–95.
[25] Mukhopadhyay A, Venugopal P, Vanka SP. Numerical study of vortex shedding from a circular cylinder in linear shear flow. J Fluids Eng 1999;121:460–8.